Journal of Alloys and Compounds 725 (2017) 544–556

Contents lists available at ScienceDirect

Journal of Alloys and Compounds

journal homepage: http://www.elsevier.com/locate/jalcom

Fabrication of double-shelled Fe_2O_3/CeO_2 boxes from CeO_2-modified Prussian blue and their enhanced performances for CO removal and water treatment

Ling Liu [a, b, *], Jingjing Shi [c], Ruiyu Wang [a, b], Hongxia Cao [c], Ziwu Liu [a, **]

[a] Low Carbon Energy Institute, China University of Mining and Technology, Xuzhou 221008, People's Republic of China
[b] Key Laboratory of Coal-Based CO_2 Capture and Geological Storage of Jiangsu Province, China University of Mining and Technology, Xuzhou 221008, People's Republic of China
[c] School of Chemical Engineering and Technology, China University of Mining and Technology, Xuzhou 221116, People's Republic of China

ARTICLE INFO

Article history:
Received 4 June 2017
Received in revised form
17 July 2017
Accepted 19 July 2017
Available online 20 July 2017

Keywords:
Ce–Fe composite oxide
Multi-shelled hollow structure
Prussian blue
Synergetic interaction
CO oxidation
Water treatment

ABSTRACT

Multiple components and well-defined complex nanostructures may synergistically enhance the performance and application of composite materials. Herein, hierarchical double-shelled Fe_2O_3/CeO_2 microboxes, with the robust Fe_2O_3 hollow microcubes inside and CeO_2 shell outside, were fabricated by a facile wet chemical process, which involved the decoration of $Fe_4[Fe(CN)_6]_3$ microcubes with CeO_2 nanoparticles, followed by the thermal decomposition of this precursor in air. The non-equilibrium heat treatment induced heterogeneous contraction process during the calcination of the $Fe_4[Fe(CN)_6]_3/CeO_2$ precursor in air, which is responsible for the formation of the unique hollow structures. The pre-deposited CeO_2 nanoparticles acted as stabilizer for the exterior surface of $Fe_4[Fe(CN)_6]_3$ cubes, and consequently played a crucial role in the formation of the unique hollow structures. The CeO_2 molar concentration of the resultant products could be tailored by simply varying the feeding amount of $Ce(NO_3)_3$. As a CO oxidation catalyst, the as-prepared Fe_2O_3/CeO_2 microboxes displayed higher catalytic activity in comparison with both CeO_2 particles and Fe_2O_3 cubes owing to the high specific surface area and the synergetic interaction between Fe_2O_3 and CeO_2. More importantly, the catalytic performance is closely associated with the component ratio between Fe_2O_3 and CeO_2. In addition, the Fe_2O_3/CeO_2 microboxes also exhibited significant adsorption capacity of Congo red, implying their potential application in water treatment.

1. Introduction

Fabrication of composite materials with complex nanostructures in a designed manner, which can bring more possibilities in tailoring the physical and chemical properties, has been regarded as a promising approach to improve their performances in different application fields [1–4]. Typically, owing to their large surface area, high pore volume, low density and available inner void space, hollow nanostructures are proposed as one of the most promising materials for the application in catalytic, electronic and biologic fields [5–7]. In particular, anisotropic hollow/porous structures with nonspherical shapes, multiple chemical compositions and complex shell architectures such as multiple layers of shells, have gained increasing attention owing to their unique structures and enhanced properties in comparison with the corresponding solid and single-component forms [8–10]. However, conventional templating methods to construct complex nonspherical hollow structures still suffer from many limitations, including the difficulty of decoration of uniform coatings on high-curvature surfaces, the lack of easy-to-use nonspherical templates and the less controllable morphology preservation during the template removal process [11,12]. Moreover, the resultant hollow structures obtained through the multistep templating approaches mostly displayed relatively simple configurations, such as single shell or/and single composition.

Metal-organic frameworks (MOFs), a typical porous multifunctional material composed of metal centers/clusters bridged by

* Corresponding author. Low Carbon Energy Institute, China University of Mining and Technology, Xuzhou 221008, People's Republic of China.
** Corresponding author.
E-mail addresses: liulingsd@gmail.com, liuling@cumt.edu.cn (L. Liu), lzwmsy@cumt.edu.cn (Z. Liu).

http://dx.doi.org/10.1016/j.jallcom.2017.07.201
0925-8388/

functional organic ligands, have attracted increasing interest due to their high porosity and large surface areas. The diverse morphologies and controllable sizes render them ideal template candidate or proper precursor for assembling hollow nanostructures, especially for non-spherical metal oxide hollow nanostructures [13–18] and metal sulfide nanostructures [19]. In comparison to other strategies, metal oxides derived from MOF templates have many distinct advantages, such as uniform size, large surface area, and hierarchical porosity.

Generally, due to the considerable weight loss, MOFs can serve as precursors to produce metal oxides hollow structures by simple thermal annealing with a proper heating rate. The gas generated by the thermal decomposition of the organic ligand and the inherent crystal growth characteristics of MOF precursor both lead to the development of porosity, while inter-diffusion may result in the formation of hollow structures. For example, Fe_2O_3 microboxes with hierarchically structured shells have been synthesized simply by annealing microcubes of Prussian blue (PB) $Fe_4[Fe(CN)_6]_3$ [20,21]. $M_xCo_{3-x}O_4$ (M = Co, Mn, Fe) porous nanocages with porous shells were synthesized by low temperature annealing of Prussian blue analogues (PBA) $M_3[Co(CN)_6]_2$ (M = Co, Mn, Fe) [22]. High symmetric porous spinel Co_3O_4 and $Zn_xCo_{3-x}O_4$ hollow polyhedral were produced by thermal decomposition of heterobimetallic zeolitic imidazolate frameworks (ZIFs) [23,24]. Fe_2O_3/Co_3O_4 double-shelled hierarchical microcubes were synthesized based on annealing of double-shelled $Fe_4[Fe(CN)_6]_3/Co(OH)_2$ microcubes, and exhibited obvious advantages as anode materials for lithium-ion battery [25].

Additionally, MOFs can be used as self-sacrificial template to fabricate various hollow structures with high complexity on basis of solid–liquid phase reaction in mild conditions. For instance, Fe_2O_3 and Fe_2O_3/MO_x (M = Sn, Si, Ge, Al, and B) microboxes were synthesized by manipulating the ion-exchange reaction between an alkaline precursor and sacrificial PB and subsequent annealing in air; then the as-formed Fe_2O_3/MO_x was etched by HCl with the preservation of the MO_x configuration [26]. Ni–Co mixed oxide nanocages were created by chemical etching Ni–Co PBA at room temperature and subsequent annealing in air [27]. Uniform $Co_3O_4/NiCo_2O_4$ double-shelled nanocages were prepared by a two-step strategy, which includes the formation of ZIF-67/Ni–Co layered double hydroxides yolk-shelled structures yolk-shelled structures with a polyhedral shape and subsequent thermal annealing in air [28].

Despite great success accomplished in the past, the rational design and controllable fabrication of well-defined complex hollow structures with both multi-shells and multi-compositions still remains a challenge, since different components with distinct physical and chemical properties could hardly be integrated simultaneously into the synthesis process. It is thus highly desirable but remains greatly challenging to fabricate hollow structures with both multi-shells and different shell compositions. To the best of our knowledge, so for there have been few reports in the synthesis of Fe–Ce binary oxide double-shelled hollow structures with different shell composition.

Herein, we demonstrated the fabrication of double-shelled Fe_2O_3/CeO_2 microboxes through the transformation of modified MOF precursor by a two-step wet chemical process, including the formation of $Fe_4[Fe(CN)_6]_3$ microcubes modified with CeO_2 nanoparticles and subsequent thermal annealing in air. The Fe_2O_3/CeO_2 microboxes possessed well-defined structures with robust Fe_2O_3 hollow microcubes inside and CeO_2 shell outside. Due to the strong interaction between CeO_2 and Fe_2O_3 and the high specific surface area, the double-shelled Fe_2O_3/CeO_2 microboxes exhibited high catalytic activity towards CO oxidation in comparison with both CeO_2 particles and Fe_2O_3 cubes. In addition, the microboxes displayed excellent adsorption performance when used to remove a common organic waste of Congo red from water, suggesting their potential application in water treatment.

2. Experimental

2.1. Materials

Polyvineypirrolydone (PVP, K-30, MW ≈ 40000), potassium hexacyanoferrate(II) trihydrate ($K_4Fe(CN)_6\cdot 3H_2O$), cerium(III) nitrate hexahydrate ($Ce(NO_3)_3\cdot 6H_2O$), hydrochloric acid (HCl), Congo red ($C_{32}H_{22}N_6O_6S_2Na_2$), hexamethylenetetramine (HMTA, $C_6H_{12}N_4$) and absolute ethanol were purchased from Sinopharm Chemical Reagent Co. Ltd. All the chemical reagents are analytically pure and used without further purification.

2.2. Synthesis of $Fe_4[Fe(CN)_6]_3$ microcubes

$Fe_4(Fe(CN)_6)_3$ microcubes were prepared according to the previous literature [20]. In a typical procedure, PVP (K-30, 3.8 g) and $K_4Fe(CN)_6\cdot 3H_2O$ (0.11 g) were dissolved in a HCl solution (0.1 M, 50 mL). After being stirred for about 30 min, a clear solution was obtained and transferred to a bottle. The bottle was then placed into an electric oven and maintained at 80 °C for 24 h. After cooling down to the room temperature, the blue precipitated powder was collected, centrifuged several times with deionized water and absolute ethanol, and finally oven-dried at 60 °C for 12 h.

2.3. Synthesis of Fe_2O_3/CeO_2 microboxes

$Fe_4[Fe(CN)_6]_3$ microcubes (0.1 g) were dispersed ultrasonically in a mixed solution of water (40 mL) and absolute ethanol (40 mL), followed by the addition of $Ce(NO_3)_3\cdot 6H_2O$ (0.15 g) and $C_6H_{12}N_4$ (0.4 g) in sequence under magnetic stirring. The suspension was further heated to 70 °C and kept refluxing for 2 h. After naturally cooling down to room temperature, the product was collected by centrifugation and washed three times with deionized water, and then oven-dried at 60 °C for 12 h. In order to obtain Fe_2O_3/CeO_2 hollow microboxes, the as-obtained precursor is then annealed at 350 °C in air for 2 h with a heating ramp of 2 °C/min. In one set of compared experiments, the total mass of $Ce(NO_3)_3\cdot 6H_2O$ was changed to 0.1 and 0.2 g, respectively, with the other experiment conditions unchanged.

2.4. Synthesis of pure Fe_2O_3 cubes

$Fe_4[Fe(CN)_6]_3$ microcubes were directly calcined at 350 °C for 3 h in air with a heating ramp of 2 °C/min.

2.5. Synthesis of pure CeO_2 particles

$Ce(NO_3)_3\cdot 6H_2O$ (0.2 g) and $C_6H_{12}N_4$ (0.4 g) was added in a mixed solution of water (40 mL) and ethanol (40 mL) in sequence. The suspension was magnetically stirred at room temperature for 30 min, and afterwards the solution was heated to 70 °C and maintained under reflux for 2 h before being cooled to room temperature. The product was collected by centrifugation and washed three times with deionized water, then dried at 60 °C in an electric oven.

2.6. Characterization

Crystallographic phases and purity were investigated by X-ray diffraction (XRD) on a Bruker D8-Advance powder X-ray diffractometer with Cu Kα radiation (λ = 0.15418 nm). Morphologies and structures were determined by scanning electron microscope (SEM) using a FEI Quanta™ 250 and transmission electron

microscope (TEM) using a FEI Tecnai G2 F20 equipped with an energy dispersive X-ray spectrometer (EDX) for elemental mapping. Thermogravimetric analyses (TG-DSC) were performed on a LABSYS EVO (SETARAM) to 700 °C under air atmosphere with a heating rate of 5 °C/min. Surface analysis was carried out with X-ray photoelectron spectroscopy (XPS, Thermo ESCALAB 250Xi) with a standard Al Kα line as the excitation source. All binding energies were corrected for surface charging by use of the C 1s peak (284.8 eV) of adventitious carbon as reference. Specific surface area measurement and porosity analysis were performed on a Quantachrome NOVA-3000 system through measuring N_2 adsorption-desorption isotherms at liquid nitrogen temperature (T = 77 K). Specific surface area and pore size were calculated by the Brunauer-Emmett-Teller (BET) method and the Barrett-Joyner-Halenda (BJH) method, respectively. Hydrogen temperature programmed reduction (H_2-TPR) experiment was performed on a PCA-1200 instrument, equipped with a thermal conductivity detector (TCD) to detect H_2 consumption. Typically, 50 mg of the sample was heated (10 °C/min) from room temperature to 700 °C in a 5 vol % H_2/Ar gaseous mixture with a flow rate of 30 mL/min. UV/Vis adsorption spectra were recorded by a Shimadzu UV-2550 spectrophotometer.

2.7. Catalytic tests

The activity measurements were carried out in a continuous flow fixed-bed micro-reactor at atmospheric pressure. In a typical experiment, 50 mg of catalyst with 500 mg silica sand were loaded into a stainless steel tube. A gas mixture of $CO/O_2/N_2$ (1/10/89 vol%) with a total flow rate of 50 mL/min flowed through the reactor. The composition of the gas exiting from the reactor was monitored with an online infrared gas analyzer (Gasboard-3100, China Wuhan Cubic Co.), which can simultaneously detect CO, CO_2 and O_2. The CO conversion ratio was calculated based on the CO consumption and CO_2 formation.

2.8. Water treatment experiment

20 mg of sample was dispersed in 20 mL of Congo red solution (the initial concentration of 100 mg/L) under magnetic stirring. After a given time, the solid and liquid were separated by centrifugation. UV–Vis absorption spectra were employed to monitor the Congo red concentration remaining in the solutions at different time intervals.

3. Results and discussion

3.1. Formation and structural analysis of Fe_2O_3/CeO_2 double-shelled boxes

Fig. 1 schematically shows the formation of Fe_2O_3/CeO_2 double-shelled microboxes by Prussian blue-based annealing reaction process. Micro-sized Prussian blue (PB, $Fe_4[Fe(CN)_6]_3$) microcrystals with a cubic shape were first created to serve as the precursor according to the previous report [20]. Next, $Fe_4[Fe(CN)_6]_3$ microcubes were dispersed into the mixed solution of water and ethanol with ultrasonication to form a homogeneous suspension. Then, a certain amount of $Ce(NO_3)_3$ and HMTA was dissolved into the above suspension in order and heated to 70 °C for 2 h in order to coat CeO_2 nanoparticles on the surface of $Fe_4[Fe(CN)_6]_3$ microcubes, as described in Equations (1) and (2). Finally, Fe_2O_3/CeO_2 double-shelled microboxes were easily produced by thermal annealing of $Fe_4[Fe(CN)_6]_3/CeO_2$ microcubes at 350 °C for 2 h in air with a ramping rate of 2 °C/min.

$$(CH_2)_6N_2 + 10\ H_2O \rightarrow 6\ HCHO + 4\ NH_4^+ + 4\ OH^- \quad (1)$$

$$2\ Ce^{3+} + 6\ OH^- + O_2 \rightarrow 2\ CeO_2 + 3\ H_2O \quad (2)$$

The detailed morphological and structural features of samples were first characterized by SEM. As shown in Fig. 2a, these $Fe_4[Fe(CN)_6]_3$ crystals consist of well-defined cubes. The surface is very smooth over the whole particle, suggesting the single-crystal-like character of the $Fe_4[Fe(CN)_6]_3$ microcubes. After the addition of a certain amount of $Ce(NO_3)_3$ to react with HMTA in a mixed solution of water and ethanol, all of the particles are still well-dispersed and inherited the morphology of the $Fe_4[Fe(CN)_6]_3$ precursor. No discrete small particles are observed. A magnified image (the inset of Fig. 2b) shows the detail of the rough surface of these microcubes, suggesting the layer by layer self-assembly of CeO_2 ultra-small nanoparticles on the surface of $Fe_4[Fe(CN)_6]_3$. After further thermal annealing at 350 °C for 2 h in air, the resultant particles are homogenous in size and retained the original cubic morphology of the precursor (Fig. 2c). Meanwhile, as revealed by the enlarged SEM image (Fig. 2d), the Fe_2O_3/CeO_2 cubes possess a rather coarse surface, which was characteristic of mesoporous materials. In addition, the Fe_2O_3 inner shell tends to distort and each side of the cubes possessed a shallow concavity due to the strong contraction during the thermal decomposition process. As shown in Fig. S1, the average sizes, estimated by the size distribution data, are 464, 548 and 424 nm for $Fe_4[Fe(CN)_6]_3$ cubes, $Fe_4[Fe(CN)_6]_3/CeO_2$ cubes and Fe_2O_3/CeO_2 boxes, respectively. The trend in size change further confirmed the surface deposition of CeO_2 components during the reflux process and the intense contraction during the heating process.

The detailed morphology of $Fe_4[Fe(CN)_6]_3/CeO_2$ cubes were further examined by TEM. The representative TEM image in Fig. 3a shows that the sample presents a solid cube structure, and no agglomerated nanocubes or scattered CeO_2 nanoparticles can be observed. Fig. 3b shows the magnified TEM image of a single cube of $Fe_4[Fe(CN)_6]_3/CeO_2$ sample, indicating that the CeO_2 shell is self-assembled together by amounts of ultra-small CeO_2 nanoparticles. The crystallographic structure and phase purity of the $Fe_4[Fe(CN)_6]_3/CeO_2$ cubes are examined by XRD. As can be seen from the XRD pattern in Fig. 3c, two types of characteristic peaks are observed. These characteristic peaks can be readily assigned to the standard cubic phase of $Fe_4[Fe(CN)_6]_3$ (JCPDS No. 01-0239) and face-centered cubic phase of CeO_2 (JCPDS No. 39-0439). No extra redundant peaks due to the other new-formed mixed phases are detected. The related peaks of CeO_2 phase seem broader compared with those of $Fe_4[Fe(CN)_6]_3$, indicating the shell is composed of smaller sized CeO_2 nanoparticles. Thermogravimetric analysis (TG-DSC) was carried out to further investigate the $Fe_4[Fe(CN)_6]_3/CeO_2$ composite precursor (Fig. 3d). The weight loss can be divided into two stages. The first one occurs in the temperature range from 100 to 250 °C, accounting for 5%, which can be assigned to the removal of the absorbed water and the residual organics. At the second one between 250 and 350 °C, a significant weight loss of 21% is observed, which results from the decomposition and oxidation of $Fe_4[Fe(CN)_6]_3$ to Fe_2O_3. The results suggest that CeO_2 nanoparticles were prone to coating around the $Fe_4[Fe(CN)_6]_3$ surface to generate a core@shell structure rather than preferential formation of separate particles. The possible reasons can be proposed as follows: (1) during the HMTA hydrolysis process, the reaction rate decreases with decreasing water concentration in the mixed water/ethanol solution, leading to reduce the nucleation and growth rate of CeO_2 [29]; (2) $Fe_4[Fe(CN)_6]_3$ possesses abundant pore channels and Fe(III) ions in $Fe_4[Fe(CN)_6]_3$ can associate with OH^- to form insoluble $Fe(OH)_3$ in alkaline solution [26], both of which may cause the enrichment of Ce^{3+} at the solid–liquid interfacial area, resulting in the preferential deposition of CeO_2 on the surface of $Fe_4[Fe(CN)_6]_3$ in the refluxing process.

The hollow interior of these Fe_2O_3/CeO_2 microboxes was

confirmed by TEM analysis. As shown in Fig. 4a, there exists sharp contrast between the shells (dark) and interior cavities (light) of the boxes, and the obvious waisted cavity is in good agreement with the result of SEM analysis. The shell framework constructed by small subunits and the interparticle mesopores distributed throughout the whole box could be observed more distinctly from the magnified TEM image (Fig. 4b). The high-resolution TEM image in Fig. 4c shows that the outer layer of Fe_2O_3/CeO_2 box is composed of amounts of ultra-small CeO_2 nanoparticles (less than 10 nm) assembled together. The shell thickness of the boxes is about 50 nm. In Fig. 4d, the lattice spacing of 0.32 nm correspond well to the characteristic (111) planes of fluorite-phase CeO_2, indicating the successful surface deposition of the CeO_2 components. EDX spectrum in Fig. 4e displays that the body of the box is composed of Fe, Ce and O elements. The Ce/(Fe + Ce) molar ratio in the as-obtained Fe_2O_3/CeO_2 microboxes is about 36.41%. The corresponding XRD pattern is shown in Fig. 4f, the peaks at $2\theta = 35.6°$, 57.3° and 62.9° are in good agreement with the characteristic (311), (511) and (440) planes of cubic Fe_2O_3 phase (JCPDS No. 39-1346); while the peaks at $2\theta = 28.5°$, 47.5°, and 56.3° correspond well to the characteristic (111), (220), and (311) planes of the face-centered cubic phase of CeO_2 structure (JCPDS No. 39-0439), respectively. No additional diffraction peaks could be observed from the XRD patterns, suggesting the completely transformation of $Fe_4[Fe(CN)_6]_3$ to the weakly crystallized Fe_2O_3 during the calcination process.

Corresponding EDX elemental mapping was employed to further examine the chemical composition component and elemental distribution of the double-shelled Fe_2O_3/CeO_2 microboxes. Fig. 5 shows the STEM image and the distribution maps of Fe, Ce, and O elements of a single Fe_2O_3/CeO_2 microbox, respectively, evidently revealing the heterogeneous distribution of Fe, Ce and O among the whole composite microcube. Fe elemental was only present in the center of the box, while Ce elemental was a typical shell feature. It is clearly indicated that the Fe_2O_3 layer is at inner shell and the CeO_2 shell is on the outer side of the Fe_2O_3/CeO_2 composite box.

To further determine the chemical composition and elemental valence states of the Fe_2O_3/CeO_2 microboxes, XPS analysis was performed and the results are shown in Fig. 6. It demonstrated clearly that the Fe_2O_3/CeO_2 microboxes contained Fe, Ce and O elements (Fig. 6a). Because of the widespread presence of carbon in the environment, the C 1s peak could also be observed clearly in their XPS survey spectrum. High-resolution of Ce 3d XPS spectrum in Fig. 6b shows the two principle binding energies of Ce $3d_{3/2}$ (U) and Ce $3d_{5/2}$ (V). Two peaks labeled as U_1 and V_1 could be assigned to characteristic of Ce(III) species, while six peaks denoted as U, U_2, U_3, V, V_2, and V_3 could be indexed to characteristic of Ce(IV); therefore, the as-prepared Fe_2O_3/CeO_2 microboxes contain the Ce^{4+} ions, along with the Ce^{3+} ions [4,30,31]. As displayed in the high-resolution XPS spectrum of Fe 2p (Fig. 6c), the peaks located at 711.4 and 725.2 eV, along with two shake-up satellite peaks at 717.9 and 732.5 eV, can be attributed to Fe^{3+}, and another two peaks centered at 710.5 and 723.8 eV can be ascribed to Fe^{2+} [32–34]. Apparently, the Fe element is present in the chemical state of Fe^{3+} and Fe^{2+}. The high-resolution spectrum for O 1s (Fig. 6d) shows two oxygen species. According to previous reports, the fitting peak at 529.3 eV is ascribed to the lattice oxygen; while the peak at 531.4 eV is corresponding to the defect or adsorbed oxygen species, such as hydroxyl, carbonate, chemisorbed oxygen or under-coordinated lattice oxygen [34–36]. The results indicate that the surface of the Fe_2O_3/CeO_2 composite box is not fully covered with CeO_2 within the detection range of XPS.

3.2. Effect factors in the formation of Fe_2O_3/CeO_2 double-shelled boxes

In this synthetic process, the pre-deposition of CeO_2 particles on the $Fe_4[Fe(CN)_6]_3$ cubes is critical to the final formation of the hierarchical Fe_2O_3/CeO_2 double-shelled boxes. As a reference, when $Fe_4[Fe(CN)_6]_3$ was first thermally decomposed to Fe_2O_3 at 350 °C and subsequently coated with a shell composed of CeO_2 nanoparticles (see the detailed synthesis procedure in the Supporting), only solid Fe_2O_3@CeO_2 core@shell cubic structures with a rather rough surface were obtained (Fig. S2 nd S3. The core@shell geometry is confirmed by the STEM line-scan spectrum (Figs. S3c and d) across a single cube, which reflects the higher atomic numbers of Fe concentrate in the center, while Ce in the outer shell of the cube. Fig. S3e shows the schematic illustration of the preparation of Fe_2O_3@CeO_2 core@shell microcubes. The result demonstrates the coated CeO_2 shell is beneficial for the heterogeneous contraction of $Fe_4[Fe(CN)_6]_3$ to fabricate the hollow structures during the heat treatment process.

Importantly, the molar ratio of Ce/(Fe + Ce) of the Fe_2O_3/CeO_2 boxes can be easily tuned by directly changing the feeding amount of $Ce(NO_3)_3$ while other conditions kept unchanged. In order to distinguish these samples, the samples with different feeding mass of $Ce(NO_3)_3$, from small to large, have been denoted as Fe_2O_3/CeO_2-0.1, Fe_2O_3/CeO_2-0.15 and Fe_2O_3/CeO_2-0.2, respectively. The Ce contents of Fe_2O_3/CeO_2-0.1 and Fe_2O_3/CeO_2-0.2 were also detected by EDX analysis (Fig. S4 and listed in Table 1, which is about 28.67% and 41.46%, respectively. The morphology and surface structure of the two samples were further investigated by TEM analysis (Fig. 7). When 0.1 or 0.2 g of $Ce(NO_3)_3$ was added to the reaction mixture, similar hollow cubic structures with rough surface were observed in the final products. The average shell thickness of the Fe_2O_3/CeO_2-0.1 and Fe_2O_3/CeO_2-0.2 was about 40 and 60 nm, respectively, indicating that the shell thickness increased with the increase of feeding molar of $Ce(NO_3)_3$. More interestingly, when 0.2 g of $Ce(NO_3)_3$ was present in the mixture solution, concave surface of the boxes no longer can be observed, indicating that the possible deposition of a much thicker CeO_2 shell which can even withstand the strong contraction during the annealing process; on the other hand, besides boxes, some yolk-shell cubic structures can also be found, as shown by arrow in Fig. 7d. Fig. S5 displays the detailed morphology and structure of a single yolk-shell cubic structure. It

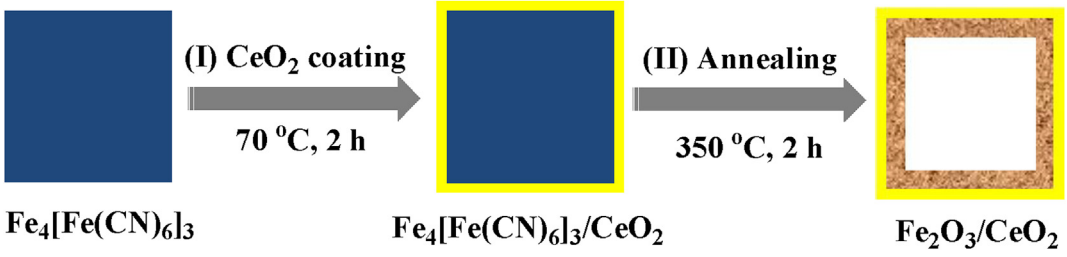

Fig. 1. Schematic illustration of the formation of Fe_2O_3/CeO_2 double-shelled microboxes.

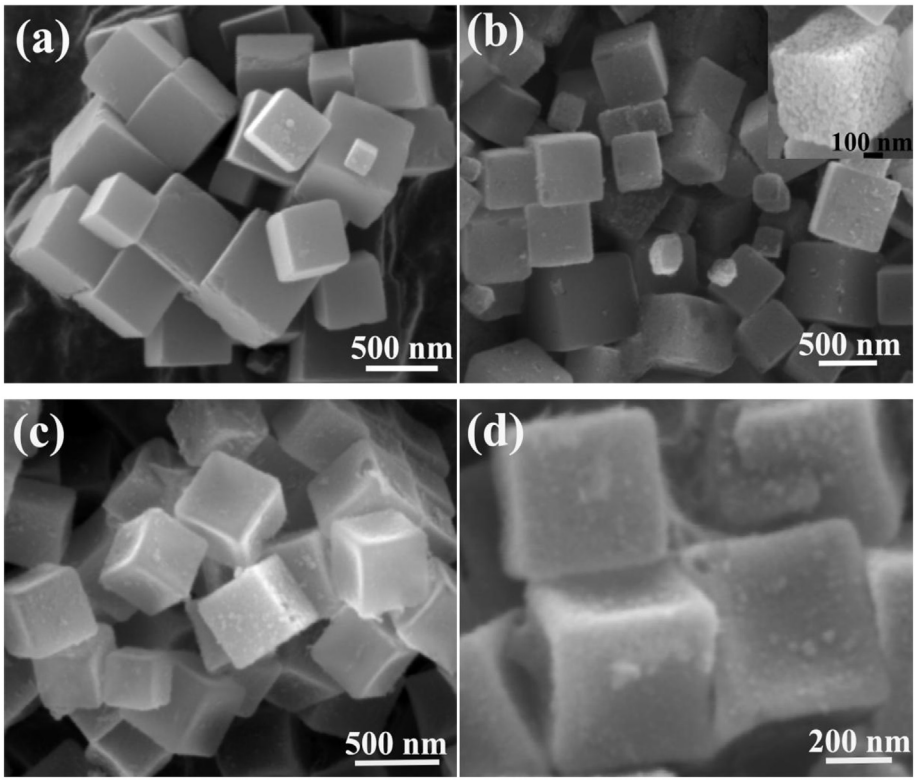

Fig. 2. SEM images of $Fe_4[Fe(CN)_6]_3$ microcubes (a), $Fe_4[Fe(CN)_6]_3/CeO_2$ microcubes (b) and Fe_2O_3/CeO_2 microboxes (c, d). The inset in panel (b) is an enlargement $Fe_4[Fe(CN)_6]_3/CeO_2$ cube.

can be clearly observed that the Fe_2O_3/CeO_2 cube possesses a two-layer box-in-box yolk-shell structure. EDX results in Fig. S5 and c present that the outer shell of the yolk-shell structure is mainly composed of Ce along with a small quantity of Fe, indicating the adhesion of some Fe_2O_3 species to the interior surface of the CeO_2 shell, while the inner shell mainly consists of Fe. In addition, the precursor of Fe_2O_3/CeO_2-0.2 sample still presents a similar solid cubic structure (Fig. S6), indicating that the morphology of $Fe_4[Fe(CN)_6]_3/CeO_2$ did not significantly change with the increase of the feeding mass of $Ce(NO_3)_3$.

3.3. Plausible formation mechanism of Fe_2O_3/CeO_2 double-shelled boxes

Generally, during the formation of the $Fe_4[Fe(CN)_6]_3$ cubes, the dissolution and recrystallization processes occur more easily on the exterior parts to reduce the defects. As a result, the interior core will be more "loose" than the exterior shell [27]. In the alkaline solution the interior defect-rich parts would be etched easily. Based on this theory, hierarchical multi-shelled $Fe(OH)_3$ microboxes have been prepared by $Fe_4[Fe(CN)_6]_3$ templating at room temperature and hydrothermal conditions, which is driven by the high concentration of hydroxide ions in an alkaline solution [26]. $Ni_3[Co(CN)_6]_2$ cages consisting of pyramid-like walls have been synthesized by treatment of $Ni_3[Co(CN)_6]_2$ cubes with ammonia due to the inhomogeneous surface reactivity of the cubes [27]. In our case, HMTA breaks down into OH and HCHO during the reflux process. Along with the hydrolysis of HMTA, the pH of the suspension changes from near neutral to slightly alkaline value [30]. Ce^{3+} is subsequently oxidized to Ce^{4+} and precipitated as CeO_2 ultra-small nanoparticles on the surface of $Fe_4[Fe(CN)_6]_3$ cubes.

With a low amount of $Ce(NO_3)_3$, hierarchical CeO_2 outside shell built up with ultra-small nanoparticles further acts as stabilizer for the exterior surface of $Fe_4[Fe(CN)_6]_3$ cubes, while the loose interior core of $Fe_4[Fe(CN)_6]_3$ cubes becomes more unstable in the weakly alkaline solution. When thermal annealing in air, at the initial stage below 350 °C, the existence of a large temperature gradient (ΔT) along the radial direction leads to the transformation of $Fe_4[Fe(CN)_6]_3$ into Fe_2O_3 in the near-surface region. During the subsequent thermally induced oxidative decomposition, the dense Fe_2O_3/CeO_2 shell is taken as a framework to prevent further contraction of the outer diameter. Two forces are exerted in opposite directions simultaneously at the interface layer between the inner $Fe_4[Fe(CN)_6]_3$ core and the dense shell. One is the cohesive force (F_c) originating from the inner $Fe_4[Fe(CN)_6]_3$ core, which induces the inner $Fe_4[Fe(CN)_6]_3$ to shrink inwardly due to the burn-off of organic components. The other is the adhesive force (F_a) coming from the pre-formed rigid Fe_2O_3/CeO_2 shell, which prevents the inward contraction of the inner $Fe_4[Fe(CN)_6]_3$. When $F_a > F_c$ in a large ΔT, the loose inner $Fe_4[Fe(CN)_6]$ continues to intensively shrink inward to the pre-formed Fe_2O_3/CeO_2 shell, accompanied by the loss of organic species in the subsequent calcination, which eventually leads to the formation of the Fe_2O_3/CeO_2 double-shelled hollow structure (Fig. 8a). The formation of the unique hollow structures is mainly based on a heterogeneous contraction process caused by the non-equilibrium heat treatment, which is essentially similar to what has been reported in the fabrication of various metal oxide hollow structures, such as Fe_2O_3 [20,37], $MnCo_2O_4$ [38], $ZnMn_2O_4$ [39], as well as many others.

However, a higher amount of $Ce(NO_3)_3$ can lead to a relatively dense rigid CeO_2 shell on the $Fe_4[Fe(CN)_6]_3$ surface. At the early stage of heat-treatment, besides the formed Fe_2O_3/CeO_2 shell, the dense CeO_2 shell may also be employed as a framework to induce the heterogeneous contraction. In this case, F_c comes from the inner $Fe_4[Fe(CN)_6]_3$, while F_a originates from the relatively dense CeO_2

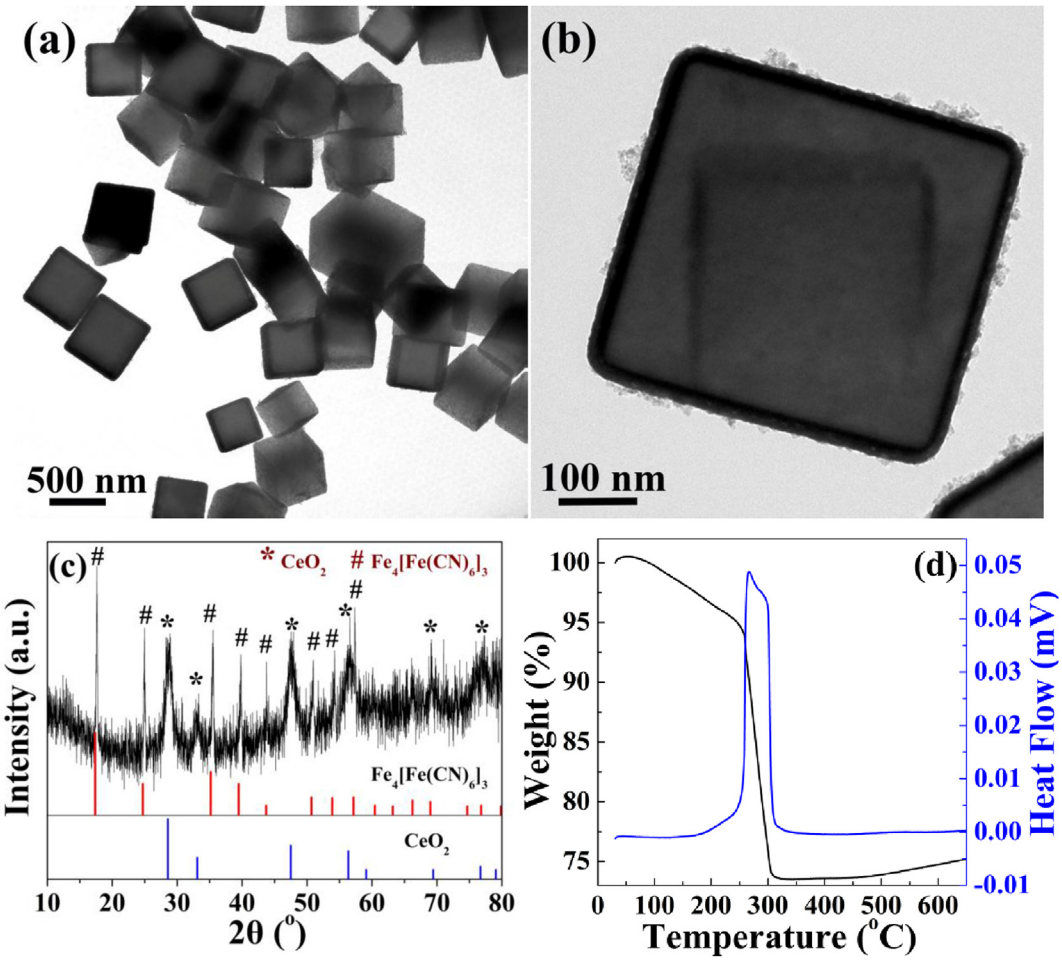

Fig. 3. TEM images (a, b), XRD pattern (c) and TG-DSC curve (d) of $Fe_4[Fe(CN)_6]_3/CeO_2$ cubes.

shell. Because F_c is obviously dominant, the inner $Fe_4[Fe(CN)_6]_3$ contracts inward and is separated from the dense CeO_2 shell in the subsequent calcination. With prolonged heating, the heterogeneous contraction process takes place on the interior $Fe_4[Fe(CN)_6]_3$ core. Based on the aforementioned shell formation and core contraction process, the inner Fe_2O_3 hollow cube is formed, producing a unique two-layer box-in-box yolk-shell structure (Fig. 8b) [40,41].

3.4. Surface properties

The N_2 adsorption-desorption isotherms and the corresponding BJH pore size distributions of the samples are present in Fig. 9. For Fe_2O_3–CeO_2 composite and Fe_2O_3 samples, the isotherms features can be classified as type IV hysteresis with a clear hysteresis loop in the relative pressure range of 0.4–1.0 due to the capillary condensation, suggesting the presence of large amount of mesopores in the samples [42,43]. Specific surface area and pore structure parameters of N_2 adsorption-desorption measurement are summarized in Table 2. The BET specific surface area (S_{BET}) is 30.69 m^2/g for Fe_2O_3 and only 13.45 m^2/g for CeO_2. However, the S_{BET} is 73.92 and 135.41 m^2/g for Fe_2O_3/CeO_2 microboxes and Fe_2O_3@CeO_2 core@shell microcubes, respectively, well above the single component. The pore size distributions of the samples are demonstrated in the inset images in Fig. 9, which were calculated from their desorption data with the BJH model. It shows a narrow pore size distribution in the range of 3–20 nm with an average pore size of about 4 nm. The total pore volume is 0.216 cm^3/g for both of the Fe_2O_3–CeO_2 composite structures, in clear contrast to 0.089 cm^3/g for Fe_2O_3 cubes and 0.030 cm^3/g for CeO_2 particles. The integration of the Fe_2O_3 and CeO_2 phases and the formation of unique hierarchical Fe_2O_3–CeO_2 composite structures through this synthesis process made an increase in both the specific surface area and the total pore volume, permitting the gas molecular to easily diffuse through the mesopores and closely contact with the active interfaces, which would be beneficial for the enhancement of catalytic performance.

In order to evaluate the reducibility of the Fe_2O_3/CeO_2 composite microstructures, H_2-TPR was investigated and the profiles are displayed in Fig. 10. For the pure CeO_2 particles, the peak at 593 °C is attributed to the reduction of the surface capping oxygen [36,44,45]. The TPR of naked Fe_2O_3 cubes presents three reduction peaks α (408 °C), β (441 °C) and γ (595 °C), which can correspond to the three-step reduction route: Fe_2O_3 → Fe_3O_4 → "FeO" → Fe^0 [46]. The H_2 consumption of the peak at 408 °C corresponds to the reduction of Fe_2O_3 to Fe_3O_4, which is generally recognized to the first reduction step of Fe_2O_3, while the two other broad reduction peaks at 441 and 595 °C can be assigned to the first conversion of Fe_3O_4 to "FeO" intermediate phases and then "FeO" to Fe^0 [47,48]. In the case of the Fe_2O_3–CeO_2 composite oxides, there are four reduction peaks in the relatively complex H_2-TPR profiles where the reduction of Fe and Ce species may overlap. Due to the decoration of CeO_2 nanoparticles on the Fe_2O_3 surface, the peak α and β obviously shift to lower temperatures, which are located at 332 and 384 °C for the Fe_2O_3/CeO_2 microboxes and at 332 and 395 °C for the

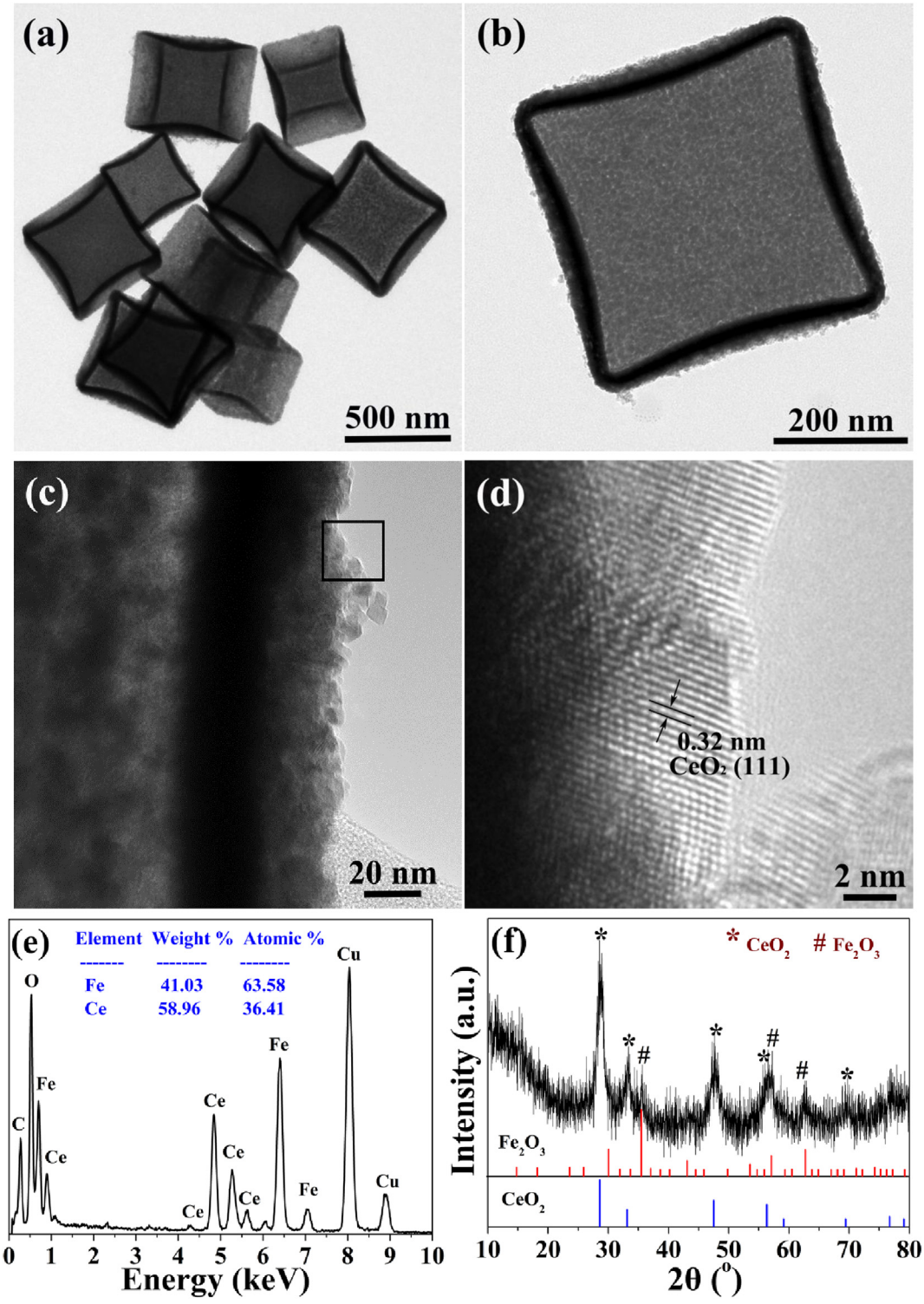

Fig. 4. TEM images (a–d), EDX spectrum (e) and XRD pattern (f) of Fe_2O_3/CeO_2 microboxes.

Fe_2O_3@CeO_2 core@shell microcubes, respectively. The broad peak γ, at 593 °C for Fe_2O_3/CeO_2 microboxes and 584 °C for Fe_2O_3@CeO_2 core@shell microcubes, can be attributed to the reduction of "FeO" intermediate species to metallic Fe and overlapping of the consumption of the surface CeO_2 [49]. Interestingly, a new reduction peak δ at 466 °C is observed, which may be related with the reduction of part of CeO_2 in intimate contact with Fe_2O_3. Consequently, the phenomena, including the shift of reduction peaks to lower temperatures and the appearance of new reduction peak, demonstrate the existence of synergetic interaction between Fe_2O_3 and CeO_2 at the two-phase interface, which could enhance the reducibility of Ce–Fe composite oxides.

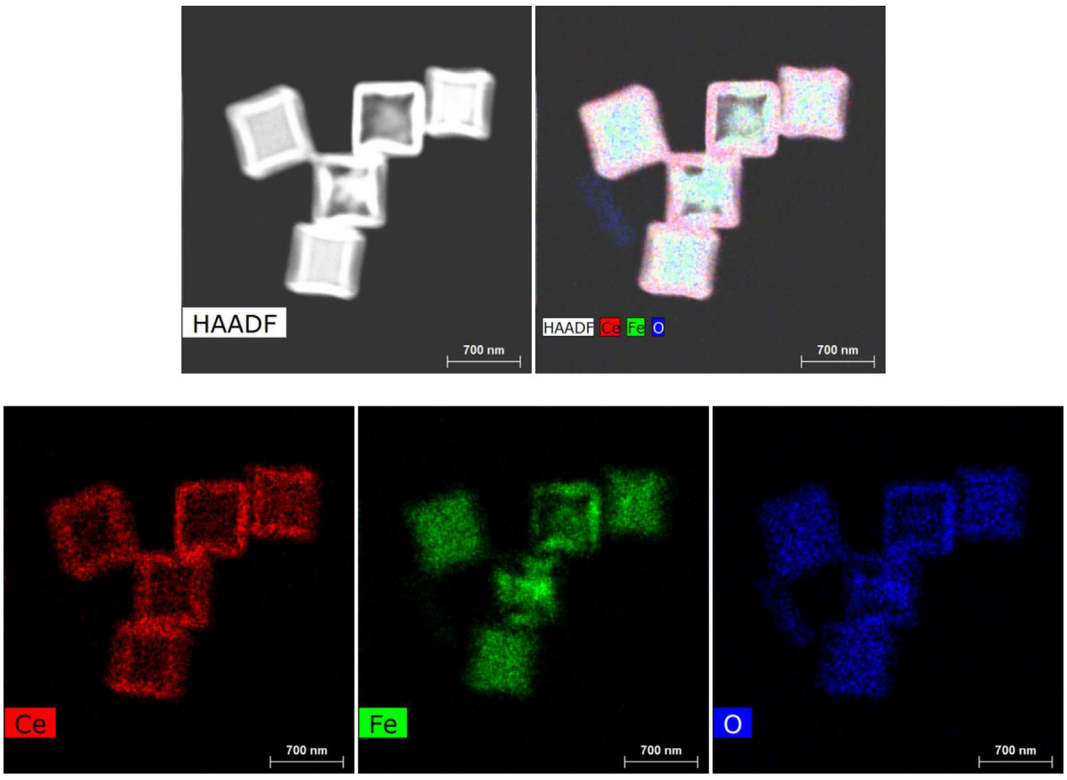

Fig. 5. STEM image of a Fe_2O_3/CeO_2 microbox and the corresponding elemental mapping of Fe, Ce and O, respectively.

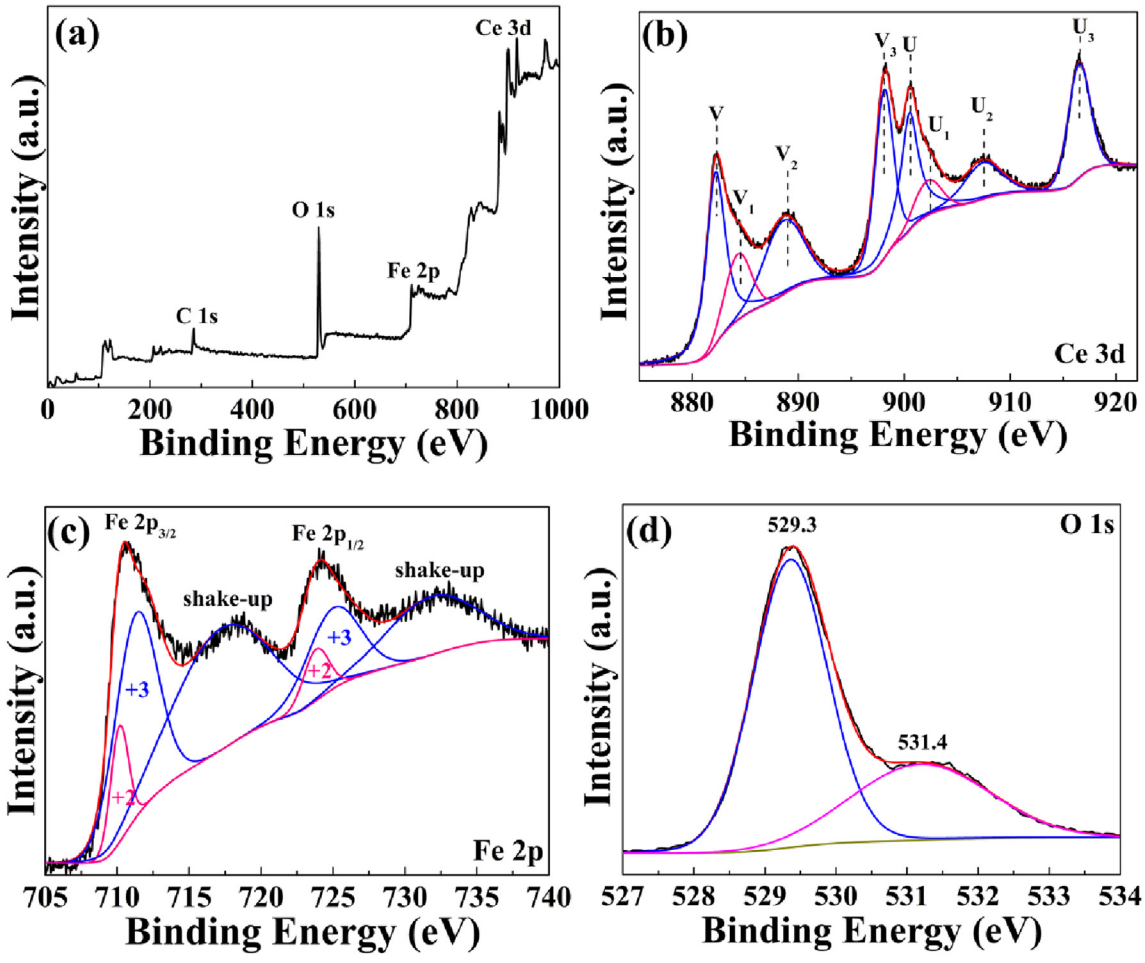

Fig. 6. XPS spectra of survey (a), Ce 3d (b), Fe 2p (c) and O 1s (d) of Fe_2O_3/CeO_2 microboxes.

Table 1
Ce/(Fe + Ce) molar ratio, shell thickness and T_{50} of the Fe_2O_3/CeO_2 hollow boxes obtained with different feeding mass of $Ce(NO_3)_3$.

Samples	Feeding mass of $Ce(NO_3)_3$ (g)	Ce/(Fe + Ce) molar ratio (%)	Average shell thickness (nm)	T_{50}[a] (°C)
Fe_2O_3/CeO_2-0.1	0.1	28.67	40	208
Fe_2O_3/CeO_2-0.15	0.15	36.41	50	195
Fe_2O_3/CeO_2-0.2	0.2	41.46	60	215

[a] Temperature for 50% CO conversion.

3.5. Catalytic performances

CO oxidation as a model reaction was carried out to evaluate the catalytic performance of the double-shelled Fe_2O_3/CeO_2 microboxes. As comparision experiments, Fe_2O_3/CeO_2 core@shell microcubes, Fe_2O_3 microcubes and CeO_2 nanoparticles were further employed to detect their catalytic activities, respectively. Fig. 11a displays the CO conversion curves of the samples by ranging reaction temperature from 100 to 320 °C. It was found that the CO conversion increases with the increase of reaction temperature for all the samples. The relative order of the catalyst activity can be evaluated by comparing the T_{100} values (the temperature at which 100% CO conversion is achieved). Amongst, T_{100} of the Fe_2O_3—CeO_2 composite structures attained at a relatively lower temperature of 230 °C, with a great decrease of 20 and 70 °C in comparison to the pure Fe_2O_3 cubes (250 °C) and CeO_2 particles (300 °C), respectively. Obviously, the Fe_2O_3—CeO_2 composite structures exhibited remarkably better CO catalytic activities. Furthermore, the light-off temperature (T_{10}) of the double-shelled Fe_2O_3/CeO_2 boxes reached as high as about 140 °C, which was increased to 160 °C for Fe_2O_3/CeO_2 core@shell cubes, indicating that the slightly higher activity of double-shelled Fe_2O_3/CeO_2 boxes at the lower temperature.

It is generally accepted that the catalytic process mainly includes the adsorption and desorption of gas molecules on the surface or at the interface during CO oxidation over metal oxide catalysts [50,51]. For composite oxide structures, the two-phase interfaces provide hybrid junctions with superior redox properties, which are favorable for achieving better activities in catalysis. Additionally, the interfaces play an important role in the binding, transport, and transformation of surface species, such as electrons and intermediates, possibly resulting in a considerable enhancement in the catalytic properties [52]. In the case of Fe_2O_3—CeO_2 heterostructures in our present study, the existence of strong synergistic interaction between the Fe_2O_3 and CeO_2 phases at the interface site modifies Fe^{3+}/Fe^{2+} and Ce^{4+}/Ce^{3+} redox cycles and increases oxygen mobility, which definitely contributes to the exceptional performance for CO oxidation. The generated oxygen vacancies from CeO_2 could also increase the adsorption amount and capture capacity for atmospheric oxygen molecules and promote the dissociation of the gas-phase oxygen into active oxygen species, thus significantly facilitating the CO oxidation reaction. In addition, the porous/hollow structure of Fe_2O_3—CeO_2 composites with a high specific surface area enables the better contact of catalytically active interface sites with the CO gas molecules, which is also favorable for the enhancement of catalytic efficiency in CO oxidation. In contrast, Fe_2O_3/CeO_2 microboxes are slightly more active than Fe_2O_3@CeO_2 core@shell microcubes, although the Fe_2O_3@-CeO_2 core@shell microcubes exhibit higher BET surface area from the BET results. The possible reasons can be summarized as follows: (1) the improved surface redox property as identified by H_2-TPR,

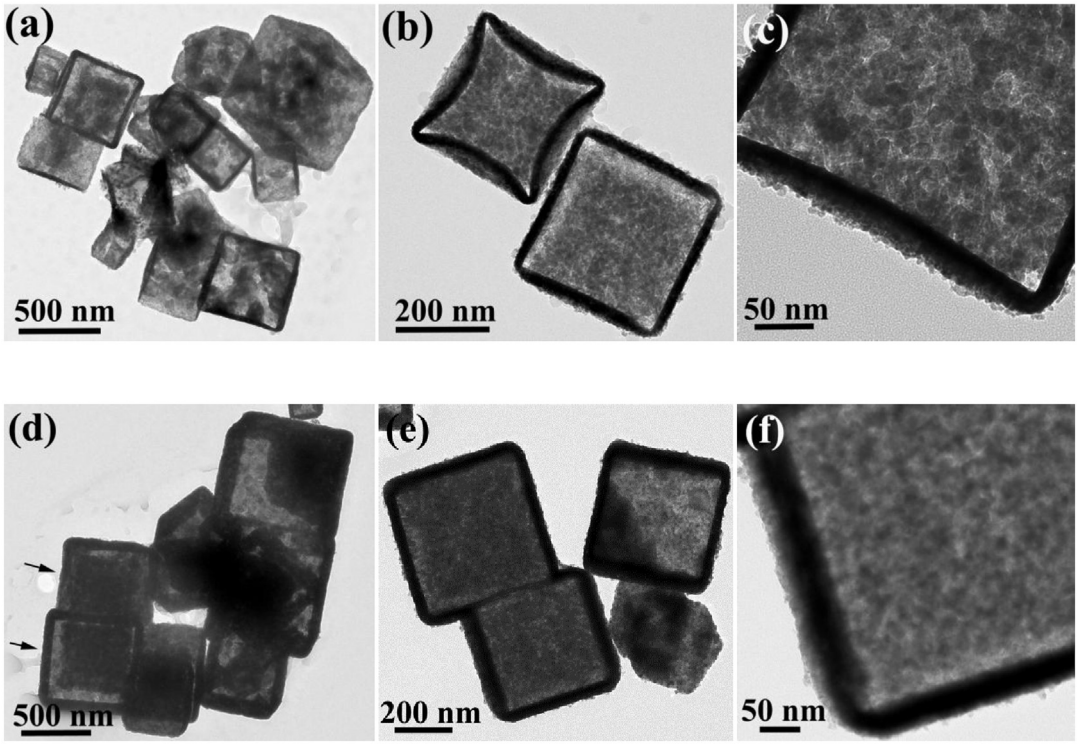

Fig. 7. TEM images of the samples of Fe_2O_3/CeO_2-0.1 (a–c) and Fe_2O_3/CeO_2-0.2 (d–f).

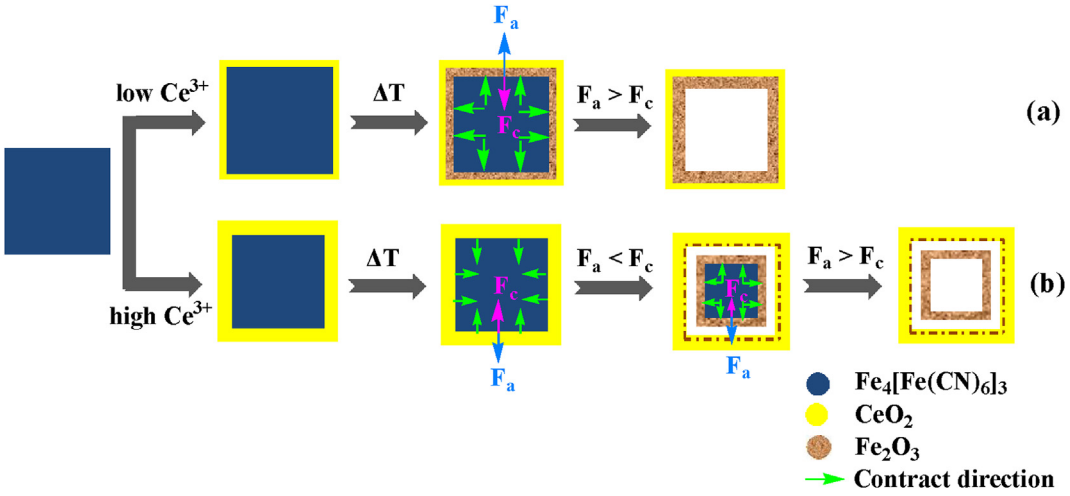

Fig. 8. Schematic illustration of the formation mechanism of Fe_2O_3/CeO_2 double-shelled boxes (a) and two-layer box-in-box yolk-shell hollow cubes (b).

which might be caused by a strong cooperative effect between CeO_2 and Fe_2O_3, resulting from the calcination process; (2) the unique hollow structure with penetrable pore channel and interior cavity, which permits the sufficient contact of the reactive sites with CO molecules and thus favors for the adsorption of reactants and desorption of products.

The CO conversion curves of the Fe_2O_3/CeO_2 boxes with different Ce molar content are comparatively described in Fig. 11b. The results indicate that the catalytic performance is closely associated with the component ratio between Fe_2O_3 and CeO_2. As shown in Table 1, the value of T_{50} is realized at 195 °C with the presence of Fe_2O_3/CeO_2-0.15, in clear contrast to 208 °C with Fe_2O_3/CeO_2-0.1 and 215 °C with Fe_2O_3/CeO_2-0.2. In comparison, both increase and decrease of the Ce molar content could cause an obvious degradation of the catalytic activity. Fe_2O_3/CeO_2-0.15 sample exhibited the highest catalytic performance among the samples. It

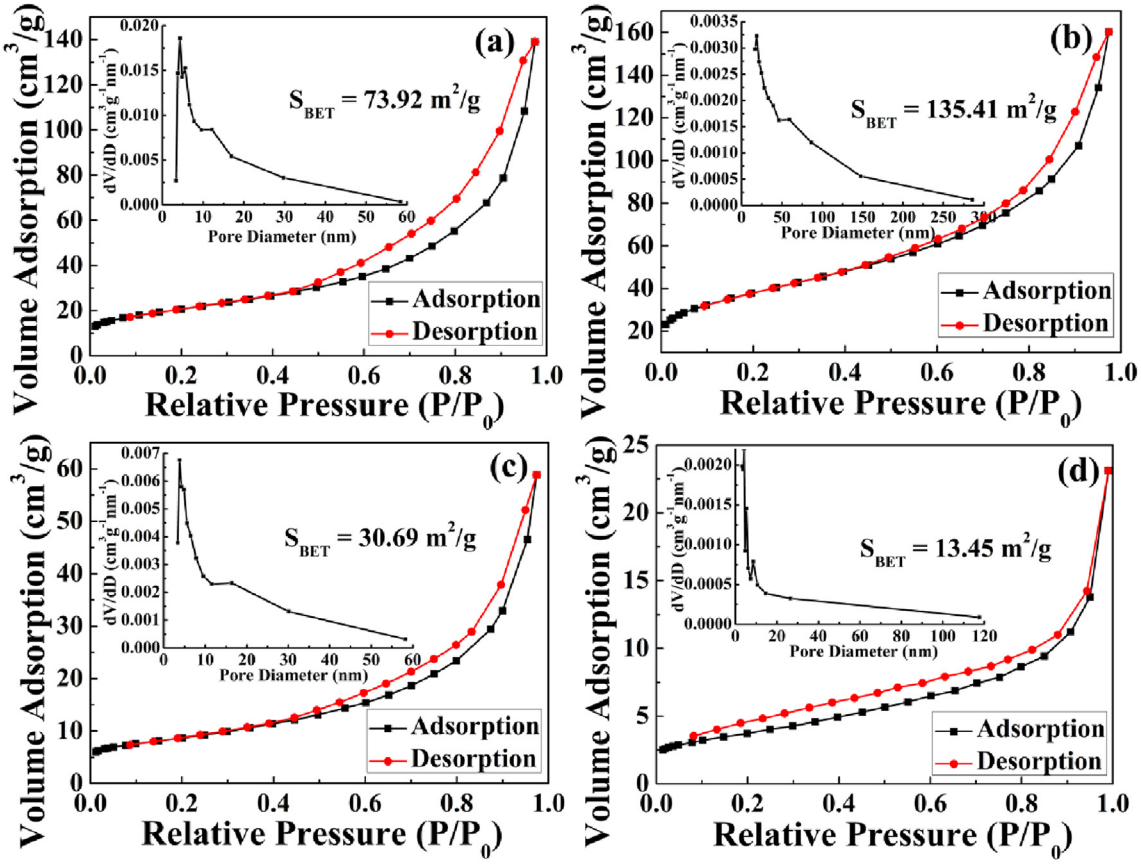

Fig. 9. Nitrogen physisorption isotherms and pore size distributions of Fe_2O_3/CeO_2 microboxes (a), Fe_2O_3@CeO_2 core@shell microcubes (b), Fe_2O_3 microcubes (c) and CeO_2 nanoparticles (d).

Table 2
Textural parameters of the Fe_2O_3–CeO_2 composites, Fe_2O_3 and CeO_2 samples.

Samples	BET surface area (m^2/g)	Pore diameter (nm)	Total pore volume (cm^3/g)
Fe_2O_3/CeO_2 double-shelled boxes	73.92	4.3	0.216
Fe_2O_3@CeO_2 core@shell cubes	135.41	3.8	0.216
Fe_2O_3 cubes	30.69	3.8	0.089
CeO_2 particles	13.45	4.1	0.030

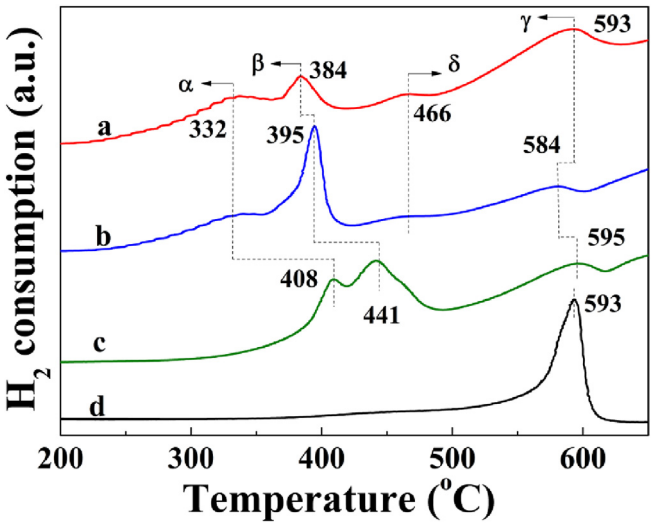

Fig. 10. H_2-TPR profiles of Fe_2O_3/CeO_2 microboxes (a), Fe_2O_3@CeO_2 core@shell microcubes (b), Fe_2O_3 microcubes (c) and CeO_2 particles (d).

can be reasonably deduced that Fe_2O_3/CeO_2-0.15 sample possesses a proper Ce molar content, larger two-phase interface area and thus makes the better contact of catalytically active interface with the CO gas molecules. Comparatively, Fe_2O_3/CeO_2-0.1 sample has the lowest Ce molar content, which means that the two-phase interface area is decreased and the synergistic reaction at the interface between CeO_2 and Fe_2O_3 is weaker than the other samples, resulting in poor activity for CO oxidation. However, with the increase of the Ce molar content, the much thicker CeO_2 shell of Fe_2O_3/CeO_2-0.2 sample may also greatly hinder the diffusion rate of CO gas molecules to the two-phase active interface site, leading to the activity decrease for CO oxidation reaction.

3.6. Water treatment performances

In general, metal oxides with pore/hollow structure could be emerged as promising adsorbents to remove organic waste from waste-water under mild conditions [53]. As an example of potential applications, the as-synthesized Fe_2O_3–CeO_2 composite microstructures were herein employed as adsorbents for the removal of Congo red species from water solution at neutral pH (Fig. 12). UV–vis absorption spectroscopy was carried out to evaluate the adsorption behavior of the Congo red solution at different time intervals. The characteristic absorption of Congo red at 488 nm was chosen to evaluate the adsorption rate of Congo red on different samples. With the increase of the treatment times, the Congo red percentage in the treated water solutions greatly decreased. The removal of the Congo red may be attributed to the electrostatic attraction between the surface of Fe_2O_3–CeO_2 composite structures and Congo red molecules [54,55]. When 20 mg of the samples were dispersed into 20 mL of the Congo red solution with the initial concentration of 100 mg/L, and subsequently the suspensions were maintained for 120 min under continuous stirring, the as-obtained Fe_2O_3–CeO_2 composite microstructures could remove above 90% of the Congo red without any additives at the room temperature. The UV/Vis absorption curves and corresponding photos at different times are shown in Fig. 12a and b, respectively. The estimated adsorption capacity of Congo red at 40 min is about 96.7 mg/g for Fe_2O_3@CeO_2 core@shell microcubes, 86.4 mg/g for Fe_2O_3/CeO_2 microboxes, 77.7 mg/g for CeO_2 nanoparticles and 6.7 mg/g for Fe_2O_3 microcubes, respectively. It was found that the as-prepared Fe_2O_3–CeO_2 composite microstructures, especially Fe_2O_3@CeO_2 core@shell microcubes, have obviously better removal ability than either CeO_2 nanoparticles or Fe_2O_3 microcubes (Fig. 12c). This might be ascribed to the high surface area and unique hierarchical core@shell or double-shelled hollow structure of the Fe_2O_3–CeO_2 composites, which can provide the plentiful active sites on the surface, leading to speed up the adsorption process [56,57]. More

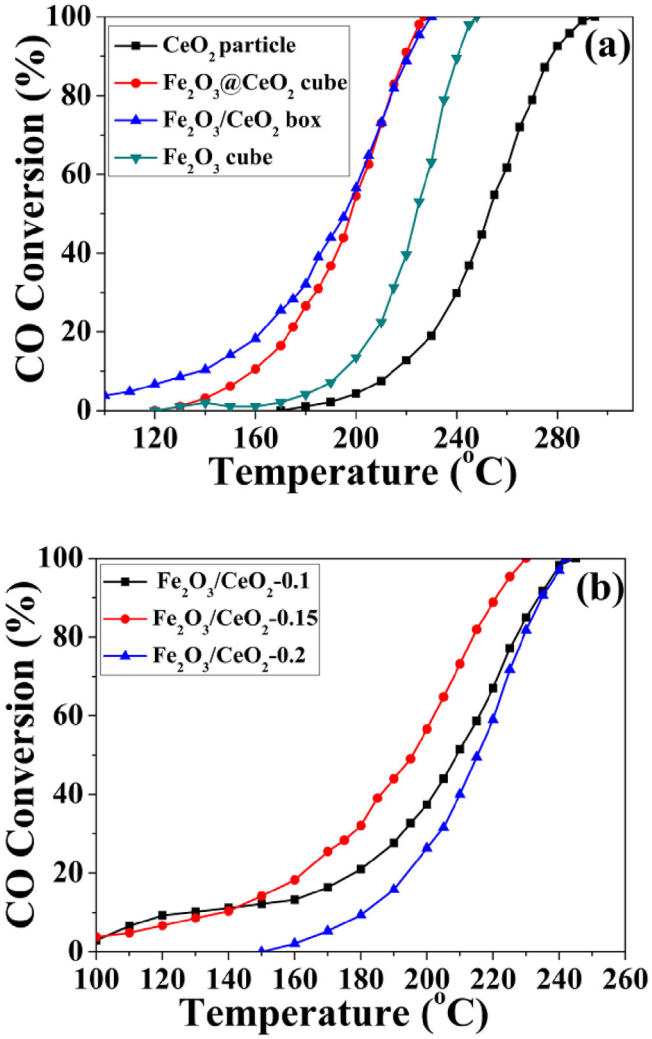

Fig. 11. (a) CO conversion curves in the presence of different samples: Fe_2O_3/CeO_2 microboxes, Fe_2O_3/CeO_2 core@shell microcubes, Fe_2O_3 microcubes and CeO_2 nanoparticles; (b) CO conversion curves of Fe_2O_3/CeO_2 microboxes with Ce molar content.

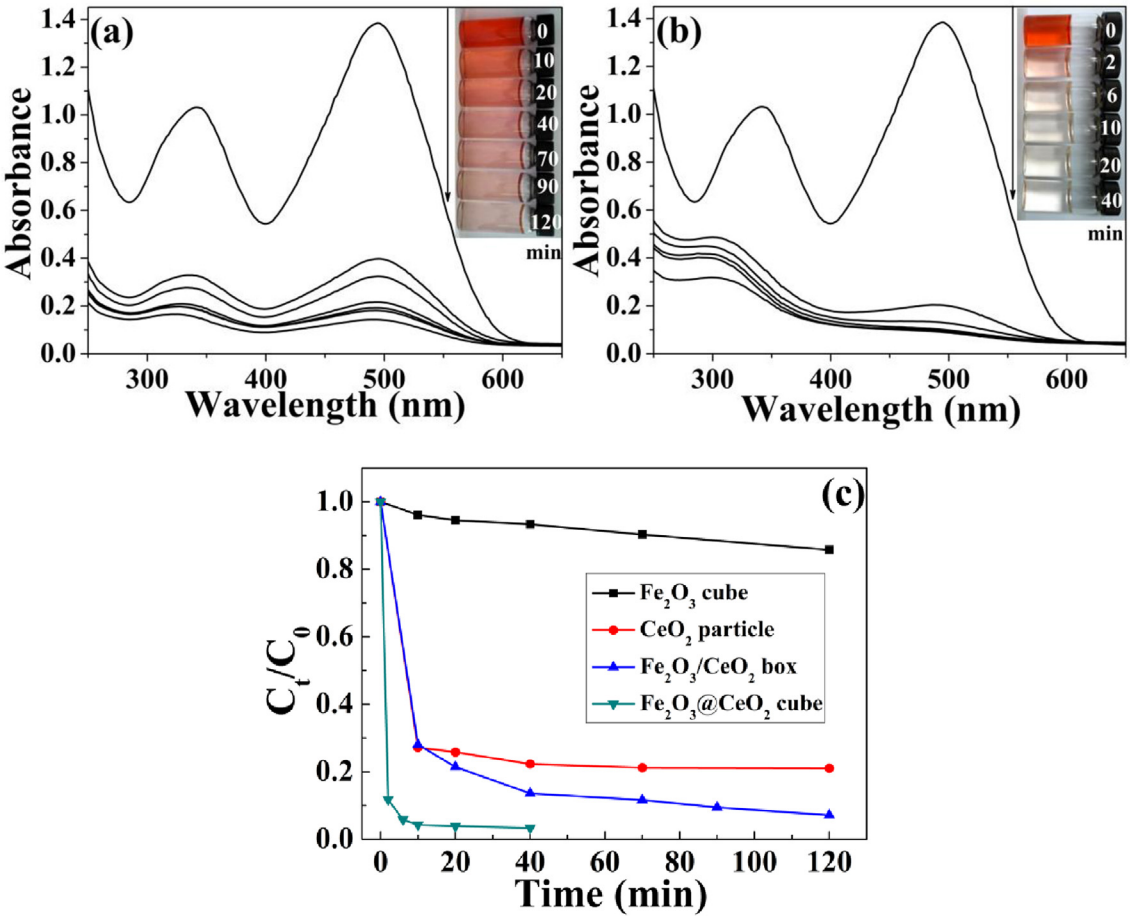

Fig. 12. UV–vis absorption spectra of Congo red solution at different time intervals in the presence of Fe_2O_3/CeO_2 microboxes (a) and Fe_2O_3/CeO_2 core@shell cubes (b). Insets display the photos of absorption of Congo red with time; (c) adsorption rate of Congo red on the different samples. C_0 is the initial concentration of the Congo red solution and C_t is the concentration of that at different intervals.

importantly, in the case of Fe_2O_3@CeO_2 core@shell cubes, abundant amount of hydroxyl groups on the surface must be retained without the need for additional heat-treatments after the CeO_2 coating process, which is definitely beneficial for the removal of Congo red on basis of the surface complexation via hydrogen bonding between the hydroxyl groups of our samples and the amine groups of Congo red molecules.

4. Conclusions

In summary, we developed a novel PB-based wet chemical approach to fabricate hierarchical double-shelled Fe_2O_3/CeO_2 microboxes. First, the ultra-small CeO_2 nanoparticles were deposited onto the surface of $Fe_4[Fe(CN)_6]_3$ cubes through a facile reflux method, and then the as-obtained $Fe_4[Fe(CN)_6]_3/CeO_2$ precursor were calcined in air at 350 °C for 2 h with a ramping rate of 2 °C/min. During the reflux process, the decorated CeO_2 nanoparticles acted as a stabilizer for the exterior surface of $Fe_4[Fe(CN)_6]_3$ cubes in the weakly alkaline solution, which was vital to the final formation of the unique hollow structures on basis of a heterogeneous contraction during the non-equilibrium heat treatment process. By varying the feeding amount of $Ce(NO_3)_3$, the molar composition of Ce and Fe in the resultant products could be easily modulated. Due to the intimate interaction between CeO_2 and Fe_2O_3 and the high specific surface area revealed by H_2-TPR and BET, the Fe_2O_3–CeO_2 composite oxide structures exhibited relatively high catalytic activity towards CO oxidation compared to both pure CeO_2 particles and Fe_2O_3 cubes. In addition, these unique hierarchical structures displayed excellent adsorption performance when employed to remove a common organic waste of Congo red from water solution, implying their potential application in wastewater treatment for the environmental protection.

Acknowledgements

This work was financially supported by the Fundamental Research Funds for the Central Universities (Grant no. 2017QNA05).

Appendix A. Supplementary data

Supplementary data related to this article can be found at http://dx.doi.org/10.1016/j.jallcom.2017.07.201.

References

[1] J. Qi, X.Y. Lai, J.Y. Wang, H.J. Tang, H. Ren, Y. Yang, Q. Jin, L.J. Zhang, R.B. Yu, G.H. Ma, Z.G. Su, H.J. Zhao, D. Wang, Chem. Soc. Rev. 44 (2015) 6749–6773.
[2] G.Q. Zhang, X.W. Lou, Angew. Chem. Int. Ed. 53 (2014) 9041–9044.
[3] M.F. Shao, M. Wei, D.G. Evans, X. Duan, Chem. Eur. J. 19 (2013) 4100–4108.
[4] W. Wei, Z.H. Wang, Z. Liu, Y. Liu, L. He, D.Z. Chen, A. Umar, L. Guo, J.H. Li, J. Power Sources 238 (2013) 376–387.
[5] Z.C. Zhang, Y.F. Chen, X.B. Xu, Y. Yang, F. Nosheen, F. Saleem, W. He, X. Wang, Angew. Chem. Int. Ed. 53 (2014) 12517–12521.
[6] Y.S. Li, J.L. Shi, Adv. Mater. 26 (2014) 3176–3205.
[7] X.Y. Lai, J.E. Halpert, D. Wang, Energy Environ. Sci. 5 (2012) 5604–5618.

[8] J. Yang, M. Cho, Y. Lee, Biosens. Bioelectron. 75 (2016) 15–22.
[9] Z.P. Li, F.C. Han, C. Li, X.L. Jiao, D.R. Chen, RSC Adv. 6 (2016) 60975–60982.
[10] Z.M. Peng, H.J. You, J.B. Wu, H. Yang, Nano Lett. 10 (2010) 1492–1496.
[11] C.H. Wang, J. Shi, X.M. Cui, H.X. Wang, J.H. Wu, C.H. Zhang, L.C. Wang, B.L. Lv, Y. Xu, J. Mater. Chem. A 4 (2016) 11000–11008.
[12] Y. Wang, P.S. Ding, X.W. Su, RSC Adv. 5 (2015) 42603–42608.
[13] K.Z. Cao, L.F. Jiao, H. Xu, H.Q. Liu, H.Y. Kang, Y. Zhao, Y.C. Liu, Y.J. Wang, H.T. Yuan, Adv. Sci. 3 (2016) 1500185.
[14] G. Huang, L.L. Zhang, F.F. Zhang, L.M. Wang, Nanoscale 6 (2014) 5509–5515.
[15] X.N. Li, Z.H. Wang, B. Zhang, A.I. Rykov, M.A. Ahmed, J.H. Wang, Appl. Catal. B Environ. 181 (2016) 788–799.
[16] L. Hua, Q.W. Chen, Nanoscale 6 (2014) 1236–1257.
[17] X.J. Cai, W. Gao, M. Ma, M.Y. Wu, L.L. Zhang, Y.Y. Zheng, H.R. Chen, J.L. Shi, Adv. Mater. 27 (2015) 6382–6389.
[18] R.B. Wu, X.K. Qian, F. Yu, H. Liu, K. Zhou, J. Wei, Y.Z. Huang, J. Mater. Chem. A 1 (2013) 11126–11129.
[19] R.B. Wu, D.P. Wang, X.H. Rui, B. Liu, K. Zhou, A.W.K. Law, Q.Y. Yan, J. Wei, Z. Chen, Adv. Mater. 27 (2015) 3038–3044.
[20] L. Zhang, H.B. Wu, S. Madhavi, H.H. Hng, X.W. Lou, J. Am. Chem. Soc. 134 (2012) 17388–17391.
[21] L. Zhang, H.B. Wu, R. Xu, X.W. Lou, CrystEngComm 15 (2013) 9332–9335.
[22] J. Wei, Y.Y. Feng, Y. Liu, Y. Ding, J. Mater. Chem. A 3 (2015) 22300–22310.
[23] R.B. Wu, X.K. Qian, X.H. Rui, H. Liu, B. Yadian, K. Zhou, J. Wei, Q.Y. Yan, X.-Q. Feng, Y. Long, L. Wang, Y.Z. Huang, Small 10 (2014) 1932–1938.
[24] R.B. Wu, X.K. Qian, K. Zhou, J. Wei, J. Lou, P.M. Ajayan, ACS Nano 8 (2014) 6297–6303.
[25] Z.Q. Li, B. Li, L.W. Yin, Y.X. Qi, ACS Appl. Mater. Interfaces 6 (2014) 8098–8107.
[26] L. Zhang, H.B. Wu, X.W. Lou, J. Am. Chem. Soc. 135 (2013) 10664–10672.
[27] L. Han, X.-Y. Yu, X.W. Lou, Adv. Mater. 28 (2016) 4601–4605.
[28] H. Hu, B.Y. Guan, B.Y. Xia, X.W. Lou, J. Am. Chem. Soc. 137 (2015) 5590–5595.
[29] R.G. Chaudhuri, S. Paria, Chem. Rev. 112 (2012) 2373–2433.
[30] S. Guo, W.Z. Sun, W.Y. Yang, Z.C. Xu, Q. Li, J.K. Shang, ACS Appl. Mater. Interfaces 7 (2015) 26291–26300.
[31] S.M. Fang, Y.J. Xin, L. Ge, C.C. Han, P. Qiu, L. Wu, Appl. Catal. B Environ. 179 (2015) 458–467.
[32] P. Sudarsanam, B. Mallesham, D.N. Durgasri, B.M. Reddy, RSC Adv. 4 (2014) 11322–11330.
[33] F.C. Zheng, D.Q. Zhu, X.H. Shi, Q.W. Chen, J. Mater. Chem. A 3 (2015) 2815–2824.
[34] L. Hu, Y.M. Huang, Q.W. Chen, J. Alloy. Compd. 559 (2013) 57–63.
[35] C. Fang, L.Y. Shi, H. Hu, J.P. Zhang, D.S. Zhang, RSC Adv. 5 (2015) 11013–11022.
[36] L. Liu, J.J. Shi, X.J. Zhang, J.Z. Liu, J. Chem. 2015 (2015) 254750.
[37] J.G. Guan, F.Z. Mou, Z.G. Sun, W.D. Shi, Chem. Commun. 46 (2010) 6605–6607.
[38] L. Liu, X.J. Zhang, J.Z. Liu, Mater. Lett. 136 (2014) 209–213.
[39] C.Z. Yuan, J.Y. Li, L.R. Hou, L.H. Zhang, X.G. Zhang, Part. Part. Syst. Charact. 31 (2014) 657–663.
[40] G.Q. Zhang, L. Yu, H.B. Wu, H.E. Hoster, X.W. Lou, Adv. Mater. 24 (2012) 4609–4613.
[41] M. Wang, F. Wang, J.P. Ma, J. Xu, J. Mater. Chem. A 2 (2014) 15480–15487.
[42] J.F. Li, S.L. Xiong, X.W. Li, Y.T. Qian, J. Mater. Chem. 22 (2012) 23254–23259.
[43] Q. Li, L.W. Yin, Z.Q. Li, X.K. Wang, Y.X. Qi, J.Y. Ma, ACS Appl. Mater. Interfaces 5 (2013) 10975–10984.
[44] D.S. Qiao, G.Z. Lu, X.H. Liu, Y. Guo, Y.Q. Wang, Y.L. Guo, J. Mater. Sci. 46 (2011) 3500–3506.
[45] J. Han, J. Meeprasert, P. Maitarad, S. Nammuangruk, L.Y. Shi, D.S. Zhang, J. Phys. Chem. C 120 (2016) 1523–1533.
[46] J. Zielinski, I. Zglinicka, L. Znak, Z. Kaszkur, Appl. Catal. A Gen. 381 (2010) 191–196.
[47] O.H. Laguna, M.A. Centeno, M. Boutonnet, J.A. Odriozola, Appl. Catal. B Environ. 106 (2011) 621–629.
[48] K.Z. Li, H. Wang, Y.G. Wei, D.X. Yan, Appl. Catal. B Environ. 97 (2010) 361–372.
[49] X. Zhu, Y.G. Wei, H. Wang, K.Z. Li, Int. J. Hydrogen Energy 38 (2013) 4492–4501.
[50] G.Z. Chen, F. Rosei, D.L. Ma, Adv. Funct. Mater. 22 (2012) 3914–3920.
[51] G.Z. Chen, Q.H. Xu, Y. Yang, C.C. Li, T.Z. Huang, G.X. Sun, S.X. Zhang, D.L. Ma, X. Li, ACS Appl. Mater. Interfaces 7 (2015) 23538–23544.
[52] H.Z. Bao, X. Chen, J. Fang, Z.Q. Jiang, W.X. Huang, Catal. Lett. 125 (2008) 160–167.
[53] B. Wang, H.B. Wu, L. Yu, R. Xu, T.-T. Lim, X. Wen, Adv. Mater. 24 (2012) 1111–1116.
[54] L.S. Zhong, J.S. Hu, H.P. Liang, A.M. Cao, W.G. Song, L.J. Wan, Adv. Mater. 18 (2006) 2426–2431.
[55] J.B. Fei, Y. Cui, X.H. Yan, W. Qi, Y. Yang, K.W. Wang, Q. He, J.B. Li, Adv. Mater. 20 (2008) 452–456.
[56] J. Cao, Y.C. Zhu, K.Y. Bao, L. Shi, S.Z. Liu, Y.T. Qian, J. Phys. Chem. C 113 (2009) 17755–17760.
[57] J. Cao, Q.H. Mao, Y.T. Qian, J. Solid State Chem. 191 (2012) 10–14.